Cao *et al. Chem. Synth.* **2025**, *5*, 3
DOI: 10.20517/cs.2024.13

Chemical Synthesis

Research Article

Open Access

Ferromagnetism of single atoms above room temperature

Yitong Cao[1,#], Xun Geng[1,#], CI Sathish[1], Mengyao Li[2], Sohail Ahmed[3], Liang Qiao[4], Xiaojiang Yu[5], Mark B. H. Breese[5], Rongkun Zheng[6], Dewei Chu[2], Jiabao Yi[1,*]

[1]Global Innovative Centre of Advanced Nanomaterials, School of Engineering, University of Newcastle, Callaghan 2308, Australia.
[2]School of Materials Science and Engineering, University of New South Wales, Kensington 2052, Australia.
[3]Aerospace and Aviation Campus, Air University, Kamra 43570, Pakistan.
[4]School of Physics, University of Electronic Science and Technology of China, Chengdu 610054, Sichuan, China.
[5]Singapore Synchrotron Light Source, National University of Singapore, Singapore 117603, Singapore.
[6]School of Physics, University of Sydney, Sydney 2006, Australia.
[#]Authors contributed equally.

Correspondence to: Dr. Jiabao Yi, Global Innovative Centre of Advanced Nanomaterials, School of Engineering, University of Newcastle, 130 University Drive, Callaghan 2308, Australia. E-mail: Jiabao.yi@newcastle.edu.au

How to cite this article: Cao, Y.; Geng, X.; Sathish, C.; Li, M.; Ahmed, S.; Qiao, L.; Yu, X.; Breese, M. B. H.; Zheng, R.; Chu, D.; Yi, J. Ferromagnetism of single atoms above room temperature. *Chem. Synth.* **2025**, *5*, 3. https://dx.doi.org/10.20517/cs.2024.13

Received: 31 Jan 2024 **First Decision:** 16 May 2024 **Revised:** 14 Aug 2024 **Accepted:** 2 Sep 2024 **Published:** 12 Dec 2024

Academic Editors: Yi Tang, Yann Garcia **Copy Editor:** Yu-Fei Wang **Production Editor:** Yu-Fei Wang

Abstract

The demands of the information era, driven by cloud computing and big data, necessitate high-density storage systems. In magnetic recording media, reducing bit size is crucial for significantly increasing areal density. Consequently, using single atoms as recording bits offers the potential to achieve unprecedented areal densities. However, achieving ferromagnetism in single atoms typically requires very low temperatures, and synthesizing large areas of single atoms for recording media remains a significant challenge. In this study, a straightforward mixing and stirring method was employed to intercalate a large number of Ni single-atoms into MoS_2 nanosheets. Remarkably, room-temperature ferromagnetism was observed in all samples. Specifically, the 2% Ni-doped MoS_2 exhibited a magnetic moment of 0.53 μ_B, which is close to the theoretical value. The magnetization depends on the bonding between nickel and sulfur atoms. In 2% Ni-doped MoS_2, nickel prefers to form Ni-S bonds, while at higher doping concentrations, S-Ni-S bonding is more prevalent, leading to antiferromagnetic coupling. The observed ferromagnetism in these higher-concentration-doped samples may be attributed to strain in the nanosheets induced by nickel intercalation or nanostructured NiS particles.

Keywords: Single-atom, MoS_2, magnetic recording media, magnetic moment

© The Author(s) 2024. **Open Access** This article is licensed under a Creative Commons Attribution 4.0 International License (https://creativecommons.org/licenses/by/4.0/), which permits unrestricted use, sharing, adaptation, distribution and reproduction in any medium or format, for any purpose, even commercially, as long as you give appropriate credit to the original author(s) and the source, provide a link to the Creative Commons license, and indicate if changes were made.

INTRODUCTION

In today's era of rapid technological advancement, we are witnessing the convergence of information technology, cloud computing and big data. The growth of information technology is remarkable, with the development and deployment of 4G, 5G, and the forthcoming 6G technologies. These advancements enable high transmission rates for streaming data and high-quality video services. One of the most popular services, cloud computing, offers on-demand data access and processing capabilities from any location at any time, relying heavily on robust data storage systems. Many companies leverage big data, both structured and unstructured, to analyze customer behavior and enhance their products or services. The vast volumes of big data generated necessitate advanced data storage solutions. Moreover, artificial intelligence (AI) and machine learning (ML) have become increasingly prevalent, and are applied extensively in research and various sectors, including industrial production, stock market predictions, transport optimization, customer habit analysis, *etc.*[1]. The development of AI technology is critically dependent on the availability of substantial data storage capabilities, as large datasets are required for effective ML.

Currently, major data storage methods include solid-state drives (SSDs), such as flash memory, and magnetic hard disk drives (HDDs). While SSDs dominate portable electronic devices such as phones and laptops, magnetic recording remains the primary medium for large-scale data storage in servers and cloud infrastructures due to its cost-effectiveness and high storage capacity[2]. Areal density, defined as the number of bits per inch (bpi) times the number of tracks per inch (tpi), is a key metric for assessing the storage capability of magnetic recording media. The bit size predominantly determines areal density: smaller recording bits yield higher storage densities and capacities. Since IBM's introduction of the RAMAC 350 with a capacity of 5 MB and an areal density of 2 Kbit/in^2 in 1955, advancements in magnetic recording media and technologies have increased storage densities to over 1.5 Tbit/in^2. Future developments in patterned recording media, where each particle serves as a recording bit, could further elevate areal densities, potentially achieving up to 500 Tbit/in^2 using single-atom recording.

Magnetic HDDs were first demonstrated by IBM (RAMAC 350) with a capacity of 5 MB and an areal density of only 2 Kbit/in^2 in 1955. With the development of advanced magnetic recording media and new technologies for recording and reading, the storage density has reached over 1.5 Tbit/in^2[3,4]. In addition, in the near future, even higher areal densities may be achievable with the advancement of patterned recording media, in which each particle serves as a recording bit[5]. To further increase the areal density, the particle size must be reduced. In the long run, the ultimate areal density of magnetic recording media is to use a single-atom as a recording bit. In this case, the areal density can reach 500 Tbit/in^2.

As a result, single-atom recording has attracted extensive interest. There are many challenges for single-atom doping, such as reading, writing, and stability of data storage, *etc*. From a material point of view alone, how to make a single-atom capable of recording data is a critical issue. It is known that ferromagnetism will change to superparamagnetism when the particle size reduces to a critical size. Then there is no remanent magnetization anymore, hence losing the ability for data storage. The starting of single-atom recording research goes back to twenty years ago, when scanning tunneling microscopy (STM) became available for manipulating a single-atom. The reversible recording of a silicon dimer was demonstrated[6]. The manipulation of a single-atom by STM has been extensively investigated[7]. For magnetic single-atom recording, a research group in IBM found that Fe and Mn single atoms can maintain a large anisotropy when deposited on copper substrate[8]. Theoretical calculations indicated that Fe and Mn atoms were embedded into a molecular network of a single layer of CuN with Cu and N atoms covalently bonded. Following the idea of possibly reducing the recording bit size using a single-atom, the magnetic properties of single atoms have been extensively investigated[9-12]. A further breakthrough was reported by ETH Zurich

scientists[13]. They used holmium (Ho) atoms adsorbed on an ultrathin MgO (100) layer deposited on an Ag (001) substrate instead of directly on an Ag substrate. A large magnetic remanence can be observed even at a temperature of 40 K. Their more recent work observed that a coercive field of 8T was obtained at 35 K and the magnetic bistability lasted a very long time[14], which is essential for magnetic data storage. However, these properties all occurred at very low temperatures.

In addition, the magnetic single-atom cannot be deposited uniformly with a large area on the surface of a substrate, which makes the areal density orders much smaller than a normal magnetic recording media. MoS_2 is a prototypical transition metal dichalcogenide with a 2D layered structure. Compared to the trigonal prismatic 2H-phase, the 1T-phase MoS_2 exhibits well-defined octahedral symmetry, which enhances its reactivity in the basal plane, thereby facilitating the anchoring of single atoms on both the edge and basal planes. Many studies have been conducted on the intercalation of transition metal single atoms into MoS_2 for applications such as water splitting[15], photocatalytic hydrogen production[16], CO_2 reduction[17] *etc*. Recently, we have synthesized a large area of Cu single atoms into MoS_2 nanosheets[18]. Based on this method, Ni was employed to be doped into MoS_2 and the ferromagnetism of Ni single atoms was investigated. The results indicated that all samples exhibited ferromagnetism above room temperature. At low doping concentrations, the Ni single-atoms demonstrate a strong magnetic moment. However, at higher doping levels, the observed ferromagnetism is primarily attributed to the strained MoS_2, where the Ni-S bonds form antiferromagnetic couplings.

EXPERIMENTAL PROCEDURE

Synthesis of 1T MoS_2

Ammonium heptamolybdate [$(NH_4)_6Mo_7O_{24}\cdot 4H_2O$], sulfur powders, hydrazine monohydrate ($N_2H_4\cdot H_2O$), sulfuric acid (H_2SO_4), and nickel powders were purchased from Sigma-Aldrich. The 1T MoS_2 was synthesized by a hydrothermal reaction, with $(NH_4)_6Mo_7O_{24}\cdot 4H_2O$ employed as the Mo source. Sulfur powders (10 mmol) and Mo source (5 mmol) were fully dissolved in 10 mL $N_2H_4\cdot H_2O$ via 20 min ultrasonication. The dissolved precursor was then put into a 100-mL stainless steel autoclave and more hydrazine monohydrate was added into the autoclave until reaching 60 mL. Then the autoclave was kept in an oven for 48 h at 180 °C. The products were sufficiently washed using 0.5M H_2SO_4 and deionized (DI) water to remove the impurities and non-react precursors. Subsequently, the final product was centrifuged at 5,000 rpm for 15 min. The centrifuged sample was then transferred into a vacuum oven to dry for 48 h at room temperature.

Synthesis of Ni single atoms of MoS_2

Nickel powders with atomic ratios of 1 at%, 2 at%, 5 at%, 10 at%, and 20 at% compared to MoS_2 nanosheets were selected and finely ground in a mortar. Afterward, they were mixed with 2 mL of hexane and placed in a small jar sealed with a magnetic stirrer. The mixed solution was magnetically stirred for seven days at room temperature under N_2 gas flow. The solution, after stirring, was then rinsed by acetone, nitric acid, ethanol, and DI water to eliminate hexane and Ni powder residues at least three times. It was then centrifuged at 1,000 rpm for 5 min to settle non-intercalated Ni residues followed by a higher-speed centrifugation at 12,000 rpm for 30 min to separate the single-atom intercalated MoS_2. Finally, the resultant paste was dried in a vacuum oven at 50 °C for 6 h. The pristine 1T-MoS_2 is labeled S0 (0 at% Ni) as a reference sample and the other variants are labeled as S1 (1 at% Ni), S2 (2 at% Ni), S5 (5 at% Ni), S10 (10 at% Ni), S20 (20 at%), respectively.

Materials characterization

The surface morphology was investigated by a FEI Nova NanoSEM 450 scanning electron microscope (SEM) at room temperature followed by an energy dispersive spectroscopy detector (EDS, Bruker SDD-EDS

detector). The crystal structure of the samples was investigated by a JEOL JEM-F200 multi-purpose transmission electron microscope (TEM) at 200 kV voltage. X-ray diffraction (XRD) analysis was carried out by a Panalytical Empyrean instrument with wavelength λ = 1.54 Å (Cu$K\alpha$) that generates at 40 kV voltage and 40 mA current. The sample was loaded onto a circular holder and the angles of measurements are within a 2θ scan range of 5° to 60°. The scan step size is 0.006° with a time-per-step of 97.92 s. Raman spectra were obtained by a Renishaw inVia Raman Microscope. A 532-nm laser source was used as the excitation source for 1 h measurement under 0.1% laser power. The coordination information is also obtained by high-energy (hard) near-edge X-ray absorption fine structure (NEXAFS) analysis in a total electron yield (TEY) mode at the Australia Synchrotron. X-ray photoelectron spectroscopy (XPS) was measured by the ThermoScientific ESCALAB 250i at UNSW, Australia. Binding energy was calibrated by the C 1s peak at 284.86 eV at room temperature. Magnetic measurement was taken by vibrating sample magnetometry attached to a physical property measure system (PPMS, Quantum Design, USA). X-ray Magnetic Circular Dichroism (XMCD) was performed at room temperature at the Singapore Synchrotron Light Source at the National University of Singapore.

RESULTS AND DISCUSSION

The Ni single-atom samples were fabricated by spontaneous incorporation of Ni single atoms in the interlayers of 1T-MoS_2 nanosheets, as reported in our previous work[18]. The intercalation of Ni single atoms was accomplished by agitating MoS_2 nanosheets prepared by a hydrothermal method and varied mass of Ni powder mixture for seven days in hexane. XRD analysis was carried out to verify both the phase distribution of MoS_2 and the intercalation of Ni single atoms. Figure 1A exhibits the XRD patterns of 1T-MoS_2 nanosheets and Ni-doped MoS_2 samples. The peaks observed at 2θ = 9.5°, 33.0°, and 57.1° correspond to the (002), (100), and (110) planes of 1T-MoS_2, respectively. Remarkably, the peak corresponding to the (002) plane shifted slightly towards a lower angle, suggesting an expansion of the interlayer following the intercalation of Ni atoms. In addition, the impurity peaks observed at 2θ = 18.4° in the S10 and S20 samples may be attributed to the leaching of S, which subsequently reacts with nickel to form NiS. The peak position corresponds to the (110) plane of NiS[19]. Raman spectroscopy was conducted to confirm whether the Ni-doped MoS_2 consistently maintained the 1T phase despite an increased dosage of intercalated atoms. Figure 1B illustrates the different phonon modes of pristine MoS_2 and intercalated MoS_2 at 154 (J_1), 219 (J_2), and 327 cm^{-1} (J_3), corresponding to the superlattice structure of semiconductor in metallic 1T phase MoS_2[20]. Likewise, the peak at 404 cm^{-1} corresponds to the A_{1g} vibration mode of 1T-MoS_2. The Raman results indicate that there was no phase transition in MoS_2 during the intercalation of Ni.

To determine the chemical composition and valence state of intercalated Ni in our samples, XPS was employed to analyze the Mo 3d and Ni 2p orbitals in pristine MoS_2 and Ni-doped MoS_2 samples. The Mo 3d spectra with different concentrations of intercalated Ni in MoS_2 are shown in Figure 1C. Two primary peaks at 229 eV and 232 eV are attributed to the $3d_{5/2}$ and $3d_{3/2}$ components of Mo^{4+}. As the concentration of Ni increases, the peak of Mo^{4+} in 1T-MoS_2 exhibits a shift towards a lower binding energy of 0.75 eV, which is consistent with that of previous studies[15,21]. Also, the proportion of 1T-MoS_2 remains consistently at 67%-76% as the concentration of intercalation increases, as shown in Supplementary Table 1. This observation underscores the stability of the 1T phase throughout the intercalation process. The Ni $2p_{3/2}$ spectra deconvolute to two peaks and their satellites, as shown in Figure 1D. For the S1 sample, no peak of Ni 2p from 71 eV to 80 eV was observed in Figure 1D. The fitting results differ from the XPS spectra of Ni in similar studies[22], where typically only one peak of Ni $2p_{3/2}$ and its satellite are observed. The presence of two peaks in the Ni $2p_{3/2}$ spectrum may be attributed to two distinct valence states of Ni species, forming bonds with sulfur atoms in the configurations of Ni-S and S-Ni-S[23]. An observable shift towards higher binding energy is noted with an increased concentration of intercalated Ni atoms, suggesting that a higher doping

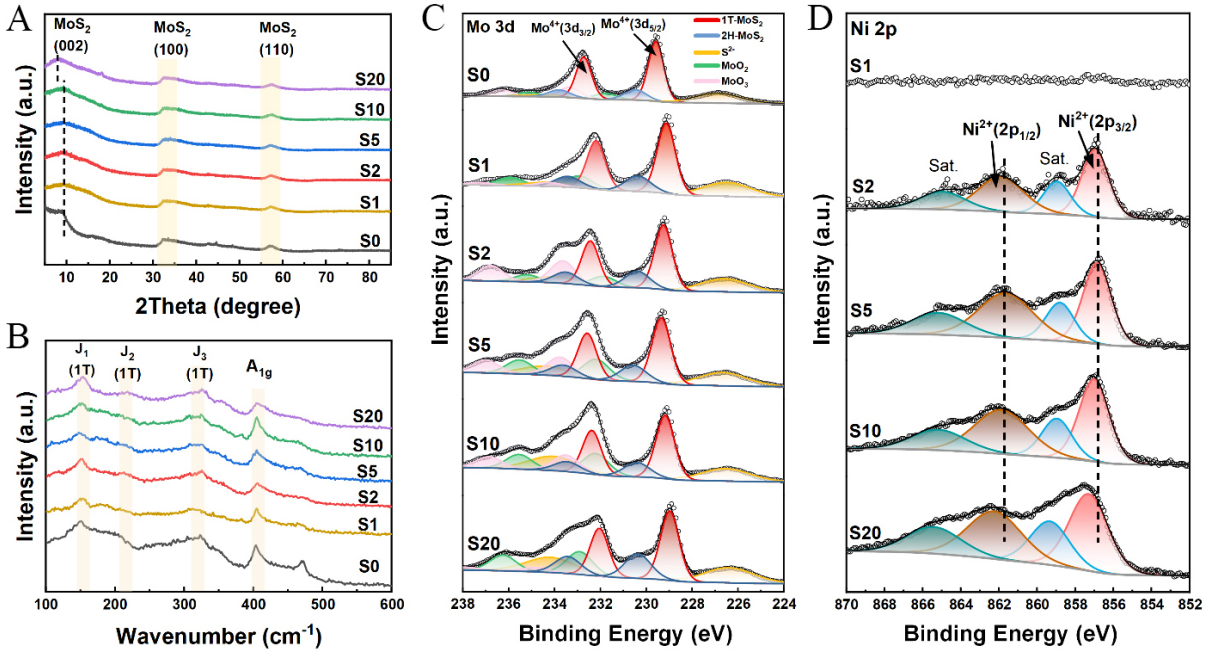

Figure 1. (A) XRD patterns of pristine 1T-dominant MoS_2 and Ni single-atom MoS_2; (B) Raman spectra of 1T-dominant MoS_2 and Ni single-atom MoS_2; (C) XPS spectra of Mo 3d; (D) XPS spectra of Ni 2p. XRD: X-ray diffraction; XPS: X-ray photoelectron spectroscopy.

level facilitates enhanced bonding with sulfur atoms.

SEM and TEM were employed for the analysis of microstructure and Ni single-atom intercalation in MoS_2 nanosheets. The SEM images of pristine MoS_2 and Ni-doped MoS_2 samples are shown in Figure 2A and Supplementary Figure 1. No significant difference can be observed among all the samples. However, when enlarging the morphology using a high-resolution TEM, the samples exhibit a nanosheets state [Figure 2B], consistent with previous studies[15,18,24]. Figure 2C exhibits the lattice of 1T-MoS_2 with a d-spacing of 0.82 nm, which is a typical distance of the MoS_2 interlayer. TEM images in Figure 2D-H depict varying concentrations of Ni intercalated MoS_2. The presence of single atoms in the interlayers of MoS_2 is evident, highlighted by yellow circles. Obviously, the single-atom concentration increases with the doping level.

However, one should note that the TEM image is very localized and only a small area of the microstructure can be examined. Hence, X-ray absorption spectroscopy (XAS) with Fourier transformation was employed to identify the single-atom state of Ni, as shown in Figure 3.

The NEXAFS region of Ni K-edge is displayed in Figure 3A, which can be divided into four regions: (1) Pre-edge region around 8,335 eV; (2) Edge area around 8,340 eV; (3) Main dipole transition peak at 8,350 eV; (4) After-edge region around 8,360 eV. Compared to Ni foil, a lower pre-edge peak is observed for Ni-doped samples, indicating higher *d-p* hybridization and an octahedral-like coordination structure. The pre-edge peak decreases further with increasing Ni concentrations [Figure 3B] and there is no significant edge shift when Ni concentration increases. This indicates the same electronegative center in all Ni single-atom-doped MoS_2 samples and the stability of Ni-centered coordination structure is improved by the formation of Ni bulk cluster in the high Ni-concentration samples (S10 and S20 samples)[25]. The peak intensity for dipole transition decreases from S1 to S5 samples, indicating a decrease in unoccupied status as the Ni concentration increases[26]. However, the peak intensity drastically increases when Ni concentration reaches

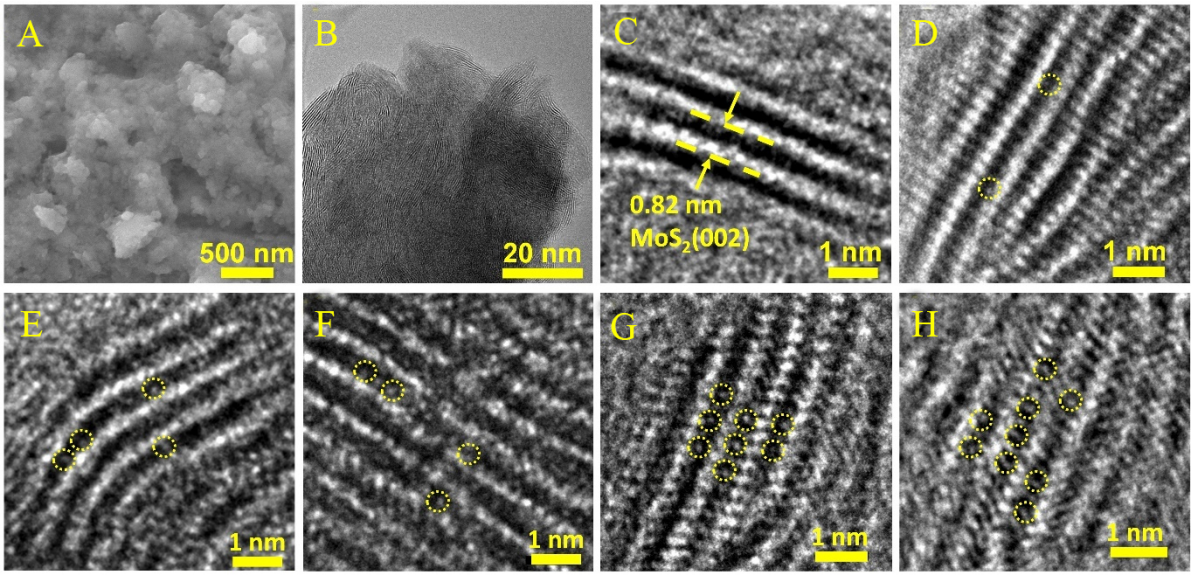

Figure 2. SEM images of pristine MoS_2 (A), TEM images of pristine MoS_2 under different magnifications (B, C) and MoS_2 with different doping concentrations of Ni: S1 (D), S2 (E), S5 (F), S10 (G), S20 (H). SEM: Scanning electron microscope; TEM: transmission electron microscope.

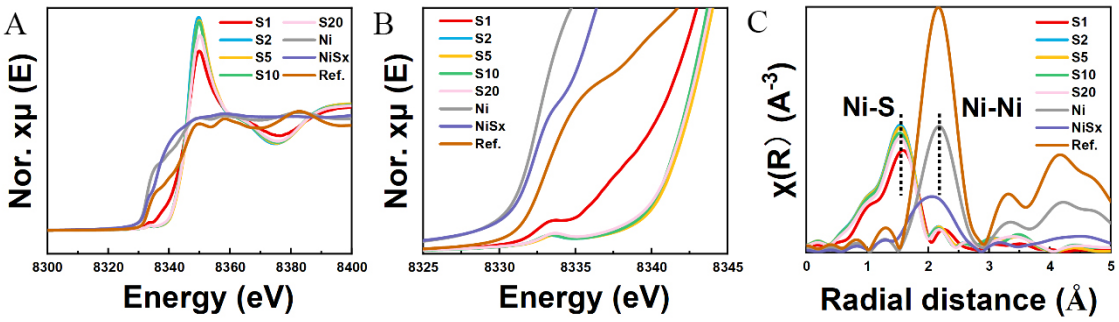

Figure 3. (A) NEXAFS curves of Ni K-edge with Ni foil reference (Ref.); (B) Zoom-in pre-edge area of Ni K-edge; (C) FT k^2-weighted NEXAFS spectra of Ni single-atom-doped MoS_2 samples. NEXAFS: Near-edge X-ray absorption fine structure; FT: fourier-transform.

10%, indicating the presence of S-rich centers around Ni atoms due to more empty orbitals. The after-edge region shows a left shift and a decreasing trend and it suggests a lower work function in high Ni concentration samples[27]. The *R*-space Fourier-transform (FT) confirms a reliable transform result with good *k*-*q* space matching, as displayed in Figure 3C and Supplementary Figure 2, respectively. Ni single-atom-doped MoS_2 samples do not exhibit obvious Ni-Ni bonds, but they show a uniform distance distribution of 1.8 Å at the first Ni-S shell. It is noticed that this value is shorter than the Ni-S bond (2.23 Å) in bulk format, indicating a single-atom distribution in Ni single-atom-doped MoS_2 samples[18]. The peak intensity decreases from S2 to S5 with a right peak shift, indicating a decreased coordination number and longer Ni-S distance due to repulsive forces between Ni-S and Mo-S chains. On the other hand, with Ni concentration increasing to 20%, the peak intensity increases with a left shift of the peak position, indicating higher coordination states and shorter Ni-S bond length due to surface aggregation[28,29].

To investigate the magnetic properties of the sample, a vibrating sample magnetometer (VSM) attached to a PPMS was employed. Initially, we measured the magnetic response of pure MoS_2, exhibiting a diamagnetic

behavior, as shown in Supplementary Figure 3. Figure 4A and B displays magnetic hysteresis loops of MoS_2 with different concentrations of Ni single atoms taken at 300 and 5 K, respectively. It is seen that all the materials show magnetic signals at room temperature and with increasing doping concentrations, the magnetization increases [Supplementary Figure 4]. In addition, with decreasing measurement temperature, the magnetization steadily increases. However, at low temperatures, paramagnetic signals become stronger, which is similar to these MoS_2 nanosheets doped with various magnetic elements or diluted magnetic semiconductors[30-32]. Figure 4C and D shows the M-H loops of the samples taken at 300 and 5 K in a small range. From the two graphs, all the samples possess a small value of coercivity, which evidences the ferromagnetic behavior of the samples. At 5 K, the coercivity becomes smaller, which is due to the strong paramagnetic signal at low temperatures. Zero field cooling (ZFC) and field cooling (FC) curves are shown in Supplementary Figure 5. All the curves indicate a paramagnetic dominated behavior, suggesting that though there may be some ferromagnetic coupling in the doped samples, most of the samples exhibit paramagnetic behaviors, suggesting the weak exchange coupling of the single atoms.

Since all the doped samples exhibit magnetic properties, it remains unclear whether the observed magnetism originates from MoS_2 or Ni, although pure MoS_2 demonstrated a diamagnetic behavior [Supplementary Figure 3]. XMCD, an element-selective technique, was employed to identify the magnetic moment associated with Ni in this study. This method allows us to determine the extent to which the Ni element contributes to the overall magnetization of the samples. The XMCD results are shown in Figure 5. It is to be noted that the Ni content (1 at%) in S1 sample is too low to produce a detectable XMCD signal. Therefore, only the spectra of four samples are presented. From the curves, it can be seen that the spectra of Ni elements in all the samples are similar[33]. Additionally, Ni in all the samples shows some magnetic moment from XMCD spectra, while the S2 sample exhibits the strongest. Using SUM rules[33,34], we can calculate the magnetic moment of Ni based on XMCD measurement. However, due to the weak XMCD signals, only the magnetic moment of S2 was accurately determined. The orbital moment of Ni in S2 is 0.02 μ_B and the spin moment is 0.51 μ_B. The overall magnetic moment is 0.53 μ_B, which is slightly lower than that of bulk Ni (0.61 μ_B). Therefore, from Figure 5, Ni contributes the majority of the magnetic moment of the S2 sample. From XMCD, Ni from S5, S10, and S20 does not contribute significant magnetic moment to the samples, while, as seen from Figure 4, the magnetization values of S5, S10 and S20 are larger than that of S2, suggesting that the magnetization is from MoS_2 nanosheets. The induced strain by the intercalation of Ni single atoms into MoS_2 nanosheets may be attributed to the magnetization[35].

Figure 6 is the description of Ni single-atom bonding when intercalated into MoS_2. At lower concentrations, Ni primarily bonds with two sulfur atoms. However, as the concentration increases, Ni bonds with four sulfur atoms, shared with molybdenum, through charge transfer, resulting in weaker bonding. This weaker bonding implies that the structure is not equivalent to a true compound. Magnetic measurements and XMCD analysis indicate that in the S2 sample, Ni primarily contributes to the magnetic moment and Ni moment is 0.51 μ_B, which is close to metallic Ni's moment, suggesting the weak bonding of Ni and S. In contrast, in samples with higher doping concentrations, the magnetic moment is likely attributed to the strained MoS_2 structure induced by the intercalation of Ni atoms. Therefore, at low doping concentrations, the bond between Ni and S resembles that in NiS_{1-x}. It is known that NiS is an antiferromagnet[36]. However, the weakly bonded Ni still presents strong magnetic moments, as measured by XMCD. At higher doping concentrations, where Ni bonds with four sulfur atoms, the resulting structure is more akin to NiS_{2-x}, which is also an antiferromagnet with a Néel temperature of 40 K[37]. Above this temperature, the material transitions to a paramagnetic state and does not exhibit ferromagnetic signals, making it difficult for XMCD to detect the magnetic moment of Ni. It is worth noting that NiS_2, despite being primarily an antiferromagnet, can occasionally display weak ferromagnetic signals due to spin frustration under certain

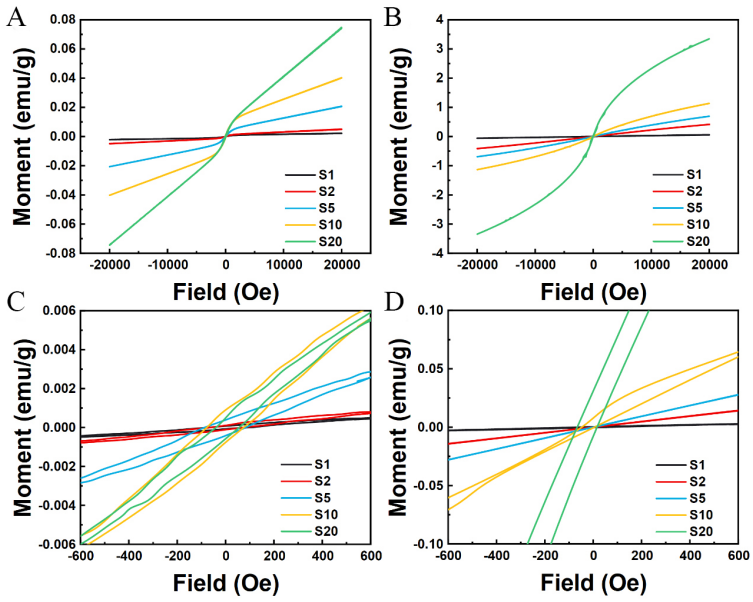

Figure 4. M-H loops of MoS_2 with different concentrations of Ni single-atoms. (A) M-H loops taken at 300 K; (B) M-H loops taken at 5 K; (C) M-H loops of A on a small scale; (D) M-H loops of B on a small scale.

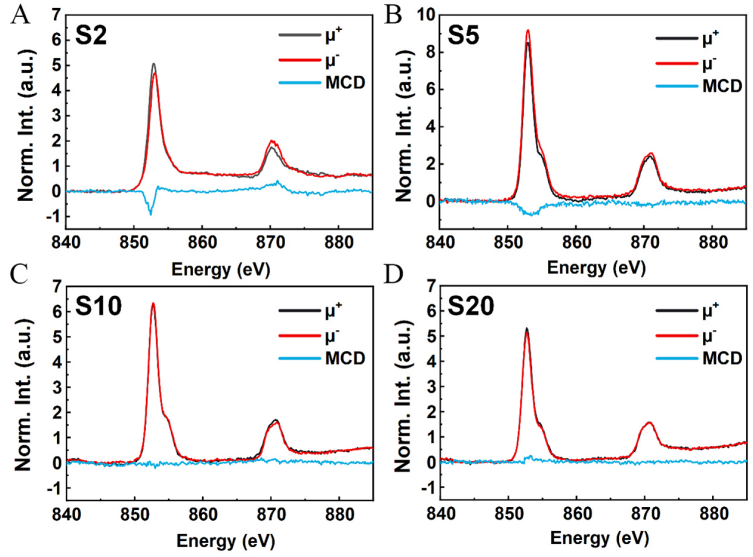

Figure 5. XAS and XMCD of the samples of MoS_2 doped with different concentrations of single-atom Ni. (A) S2; (B) S5; (C) S10; (D) S20. XAS: X-ray absorption spectroscopy; XMCD: X-ray magnetic circular dichroism.

conditions[38]. On the other hand, from XRD analysis, for higher doping concentration samples, i.e., S20, the NiS peak could be observed. Nanostructured NiS may contributed significantly to the magnetization at low temperatures due to spin frustration. Furthermore, as discussed previously, the high doping concentration of Ni may induce strain in the MoS_2 nanosheets, leading to magnetic behavior[35].

CONCLUSIONS

In this work, a straightforward mixing and stirring method was employed to synthesize Ni single-atom

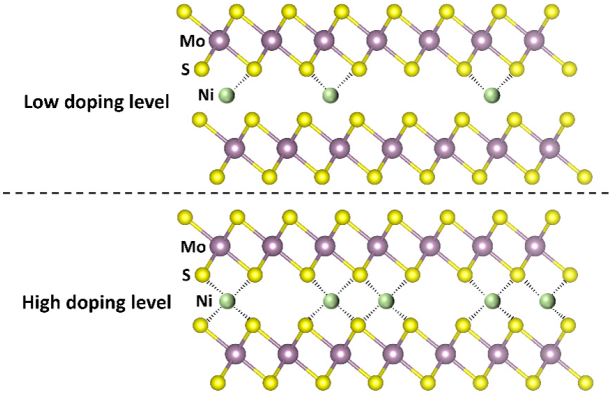

Figure 6. Possible doping configuration of Ni-MoS_2.

intercalated MoS_2 nanosheets. Single-atom doping has been confirmed by high-resolution TEM and XAS with Fourier transformation. All the Ni single-atom-doped MoS_2 samples exhibited room temperature ferromagnetism. However, the ferromagnetism observed in samples other than the 2% Ni-doped ones is primarily attributed to the strain in MoS_2 induced by the intercalation of Ni single atoms. The nature of the bonding formed by the single atoms significantly influences the magnetic coupling. To advance single-atom recording technology, further research should focus on the bonding environment of these single-atoms.

DECLARATIONS

Authors' contributions

Supervised the project: Yi J
Made materials characterization, data analysis and wrote the manuscript: Cao Y, Geng X
Measured the magnetic properties: Sathish CI
Performed the XPS, Raman and TEM experiment: Li M, Chu D
Conducted XMCD measurement: Yu X, Breese MBH
Carried out XAS measurement and contributed to the sample characterization: Geng X, Zheng R
Performed UPS measurement: Qiao L
Assisted with characterization and analysis of magnetic properties: Ahmed S
All authors contributed to the revision of the manuscript.

Availability of data and materials

The rata data supporting the findings of this study are available within its Supplementary Materials. Further data are available from the corresponding author upon reasonable request.

Financial support and sponsorship

This work was supported by the Australian Research Council (DP220103045). The authors would like to acknowledge the Singapore Synchrotron Light Source for providing the facility necessary for conducting the research. The Laboratory is a National Research Infrastructure under the National Research Foundation, Singapore. Any opinions, findings and conclusions or recommendations expressed in this material are those of the author(s) and do not reflect the views of National Research Foundation, Singapore.

Conflicts of interest

All authors declared that there are no conflicts of interest.

Ethical approval and consent to participate

Not applicable.

Consent for publication

Not applicable.

Copyright

© The Author(s) 2024.

REFERENCES

1. Stephen P. Storage requirements for AI, ML and analytics in 2022. Available from: https://www.computerweekly.com/feature/Storage-requirements-for-AI-ML-and-analytics-in-2022. [Last accessed on 12 Dec 2024].
2. Hsu, W. H.; Victora, R. H. Heat-assisted magnetic recording - micromagnetic modeling of recording media and areal density: a review. *J. Magn. Magn. Mater.* **2022**, *563*, 169973. DOI
3. Heat assisted magnetic recording (HAMR). Available from: https://www.seagate.com/au/en/innovation/hamr/. [Last accessed on 6 Sep 2024].
4. Thomas, C. A new phase of magnetic recording. Available from: https://www.forbes.com/sites/tomcoughlin/2024/01/20/a-new-phase-of-magnetic-recording/?sh=6572f395129d. [Last accessed on 6 Sep 2024].
5. Ross, C. Patterned magnetic recording media. *Annu. Rev. Mater. Res.* **2001**, *31*, 203-235. DOI
6. Quaade, U. J.; Stokbro, K.; Lin, R.; Grey, F. Single-atom reversible recording at room temperature. *Nanotechnology* **2001**, *12*, 265-272. DOI
7. Morgenstern, K.; Lorente, N.; Rieder, K. H. Controlled manipulation of single atoms and small molecules using the scanning tunnelling microscope. *Physica. Status. Solidi.* **2013**, *250*, 1671-1751. DOI
8. Hirjibehedin, C. F.; Lin, C. Y.; Otte, A. F.; et al. Large magnetic anisotropy of a single atomic spin embedded in a surface molecular network. *Science* **2007**, *317*, 1199-1203. DOI PubMed
9. Meier, F.; Zhou, L.; Wiebe, J.; Wiesendanger, R. Revealing magnetic interactions from single-atom magnetization curves. *Science* **2008**, *320*, 82-86. DOI PubMed
10. Khajetoorians, A. A.; Lounis, S.; Chilian, B.; et al. Itinerant nature of atom-magnetization excitation by tunneling electrons. *Phys. Rev. Lett.* **2011**, *106*, 037205. DOI PubMed
11. Donati, F.; Dubout, Q.; Autès, G.; et al. Magnetic moment and anisotropy of individual Co atoms on graphene. *Phys. Rev. Lett.* **2013**, *111*, 236801. DOI
12. Rau, I. G.; Baumann, S.; Rusponi, S.; et al. Reaching the magnetic anisotropy limit of a 3D metal atom. *Science* **2014**, *344*, 988-992. DOI
13. Donati, F.; Rusponi, S.; Stepanow, S.; et al. Magnetic remanence in single atoms. *Science* **2016**, *352*, 318-321. DOI PubMed
14. Natterer, F. D.; Donati, F.; Patthey, F.; Brune, H. Thermal and magnetic-field stability of holmium single-atom magnets. *Phys. Rev. Lett.* **2018**, *121*, 027201. DOI PubMed
15. Li, M.; Cai, B.; Tian, R.; et al. Vanadium doped 1T MoS_2 nanosheets for highly efficient electrocatalytic hydrogen evolution in both acidic and alkaline solutions. *Chem. Eng. J.* **2021**, *409*, 128158. DOI
16. Chu, X.; Sathish, C. I.; Li, M.; et al. Anti-Stoke effect induced enhanced photocatalytic hydrogen production. *Battery. Energy.* **2023**, *2*, 20220041. DOI
17. Singh, S.; Modak, A.; Pant, K. K.; Sinhamahapatra, A.; Biswas, P. MoS_2-nanosheets-based catalysts for photocatalytic CO_2 reduction. *ACS. Appl. Nano. Mater.* **2021**, *4*, 8644-8667. DOI
18. Li, M.; Selvarajan, P.; Wang, S.; et al. Thermostable 1T-MoS_2 nanosheets achieved by spontaneous intercalation of Cu single atoms at room temperature and their enhanced HER performance. *Small. Struct.* **2023**, *4*, 2300010. DOI
19. Ma, Z.; Yuan, X.; Zhang, Z.; et al. Novel flower-like nickel sulfide as an efficient electrocatalyst for non-aqueous lithium-air batteries. *Sci. Rep.* **2015**, *5*, 18199. DOI PubMed PMC
20. Attanayake, N. H.; Thenuwara, A. C.; Patra, A.; et al. Effect of intercalated metals on the electrocatalytic activity of 1T-MoS_2 for the hydrogen evolution reaction. *ACS. Energy. Lett.* **2017**, *3*, 7-13. DOI
21. Liu, Z.; Yu, X.; Li, J.; et al. Electrocatalytic hydrogenation of indigo by NiMoS: energy saving and conversion improving. *Dalton. T.* **2023**, *52*, 17438-17448. DOI PubMed
22. Panchu, S. J.; Raju, K.; Singh, P.; Johnson, D. D.; Swart, H. C. High mass loading of flowerlike Ni-MoS_2 microspheres toward efficient intercalation pseudocapacitive electrodes. *ACS. Appl. Energy. Mater.* **2023**, *6*, 2187-2198. DOI
23. Liao, W.; Pang, S.; Wang, S.; Su, H.; Zhang, Y. vs-NiS2/NiS Heterostructures achieving ultralow overpotential in alkaline hydrogen evolution. *Langmuir* **2022**, *38*, 13916-13922. DOI PubMed
24. Li, M.; Zhou, Z.; Hu, L.; et al. Hydrazine hydrate intercalated 1T-dominant MoS_2 with superior ambient stability for highly efficient electrocatalytic applications. *ACS. Appl. Mater. Inter.* **2022**, *14*, 16338-16347. DOI
25. Jiang, J.; Sun, F.; Zhou, S.; et al. Atomic-level insight into super-efficient electrocatalytic oxygen evolution on iron and vanadium Co-

doped nickel (oxy)hydroxide. *Nat. Commun.* **2018**, *9*, 2885. DOI PubMed PMC

26. Baker, M. L.; Mara, M. W.; Yan, J. J.; Hodgson, K. O.; Hedman, B.; Solomon, E. I. K- and L-edge X-ray absorption spectroscopy (XAS) and resonant inelastic X-ray scattering (RIXS) determination of differential orbital covalency (DOC) of transition metal sites. *Coordin. Chem. Rev.* **2017**, *345*, 182-208. DOI PubMed PMC
27. Guda, A. A.; Guda, S. A.; Martini, A.; et al. Understanding X-ray absorption spectra by means of descriptors and machine learning algorithms. *NPJ. Comput. Mater.* **2021**, *7*, 203. DOI
28. Kerr, B. V.; King, H. J.; Garibello, C. F.; et al. Characterization of energy materials with X-ray absorption spectroscopy-advantages. *Energ. Fuel.* **2022**, *36*, 2369-2389. DOI
29. Newville, M. Fundamentals of XAFS. *Rev. Mineral. Geochem.* **2014**, *78*, 33-74. DOI
30. Ahmed, S.; Ding, X.; Bao, N.; et al. Inducing high coercivity in MoS_2 nanosheets by transition element doping. *Chem. Mater.* **2017**, *29*, 9066-9074. DOI
31. Ma, Y. W.; Yi, J. B.; Ding, J.; Van, L. H.; Zhang, H. T.; Ng, C. M. Inducing ferromagnetism in ZnO through doping of nonmagnetic elements. *Appl. Phys. Lett.* **2008**, *93*, 042514. DOI
32. Ahmed, S.; Ding, X.; Murmu, P. P.; et al. High coercivity and magnetization in WSe_2 by codoping Co and Nb. *Small* **2020**, *16*, e1903173. DOI
33. Ding, X.; Cui, X.; Tseng, L. T.; et al. Realization of high magnetization in artificially designed Ni/NiO layers through exchange coupling. *Small* **2023**, e2304369. DOI
34. Saadaoui, H.; Luo, X.; Salman, Z.; et al. Intrinsic ferromagnetism in the diluted magnetic semiconductor Co-TiO2. *Phys. Rev. Lett.* **2016**, *117*, 227202. DOI
35. Ren, H.; Xiang, G. Strain-modulated magnetism in MoS_2. *Nanomaterials* **2022**, *4*, 1929. DOI PubMed PMC
36. Panda, S. K.; Dasgupta, I.; Şaşıoğlu, E.; Blügel, S.; Sarma, D. D. NiS - an unusual self-doped, nearly compensated antiferromagnetic metal. *Sci. Rep.* **2013**, *3*, 2995. DOI PubMed PMC
37. Barthelemy, E.; Chavant, C.; Collin, G.; Gorochov, O. Metal-non metal transition of Ni1-s and NiS substituted by Se, As and Fe: transport properties and structural aspect. *Journal. De. Physique.* **1976**, *10*, C4-17. DOI
38. Kikuchi, K.; Miyadai, T.; Ito, Y. Weak ferro- and antiferromagnetism of NiS_2. *J. Magn. Magn. Mater.* **1980**, *15*, 485-6. DOI